Article

Investigation of Electromagnetic Losses Considering Current Harmonics in High-Speed Permanent Magnet Synchronous Motor

Ju-Hyeong Lee [1], Soyoung Sung [2], Han-Wook Cho [3], Jang-Young Choi [4],* and Kyung-Hun Shin [1],*

[1] Department of Power System Engineering, Chonnam National University, Yeosu 59626, Republic of Korea
[2] Alternative Fuels and Power System Research Center, Korea Research Institute of Science and Ocean Engineering, Daejeon 34103, Republic of Korea
[3] Department of Electric, Electronic, and Communication Engineering Education, Chungnam National University, Daejeon 34134, Republic of Korea
[4] Department of Electrical Engineering, Chungnam National University, Daejeon 34134, Republic of Korea
* Correspondence: choi_jy@cnu.ac.kr (J.-Y.C.); kshin@jnu.ac.kr (K.-H.S.)

Abstract: This paper presents a characteristic analysis and experimental verification for predicting the electromagnetic losses in high-speed permanent magnet synchronous motors. To predict the operating characteristics (such as speed and input current), dynamic modeling is conducted that combines models for the space vector pulse width modulation (SVPWM) inverter and high-speed permanent magnet synchronous motor (HPMSM). By applying the predicted harmonic currents to the electromagnetic analysis, DC and AC copper losses of the stator winding, and eddy current loss of the rotor sleeve and rotor permanent magnet, are comprehensively analyzed using the finite element (FE) method. In particular, by analyzing the magnetic field behavior of magnetic flux density according to harmonics, a core loss analysis technique was presented. The validity of the hybrid analysis, which combines the stator copper loss and rotor eddy current loss derived from the FE analysis and the proposed core loss analysis, was verified through comparison with the experimental results under various operating conditions. Compared with the experimental results, the error of total losses using the hybrid analysis with a sinusoidal current was about 47.39%, and total losses using the hybrid analysis with a harmonic current was significantly improved to within 3.7%.

Keywords: dynamic modeling; electromagnetic losses; experimental verification; high-speed permanent magnet synchronous motor

1. Introduction

High-speed permanent magnet synchronous motors (HPMSMs) are widely employed in direct drive applications (such as compressors, gas turbines, distributed power generation, and flywheels) due to their advantages of system compactness, high specific power, high efficiency, light weight, and easy maintenance [1]. However, when developing the HPMSM, design, optimization, and multidisciplinary analysis processes considering operating temperature, reliability, efficiency, and maintainability are required [2]. Moreover, an accurate prediction of electromagnetic losses is essential to analyze the efficiency, accurate operating temperature, insulation stability, and demagnetization of the permanent magnet (PM) [1–3]. Electromagnetic losses consist of core losses in the stator core, copper losses in the stator winding, and eddy current losses in the rotor sleeve and PM, which are conductive materials. These electromagnetic losses increase significantly in HPMSMs due to their high operating frequency, magnetomotive force (MMF) harmonics of the stator winding current, slotting effect, and time harmonics of the stator current caused by the pulse width modulation (PWM) inverter [4–7]. Although the magnitude of the harmonic components is lower than that of the fundamental components, since the harmonic frequencies are high,

the electromagnetic losses caused by the harmonics have a significant effect on overall electromagnetic losses.

This paper presents a comprehensive analysis of the stator core losses, stator copper losses, and rotor eddy current losses of HPMSMs considering the harmonic current supplied from the space vector PWM (SVPWM) inverter. First, to predict the harmonic current generated from the SVPWM inverter, a mathematical model combining the HPMSM modeling (based on the electromagnetic circuit parameters) and the SVPWM inverter results is established using MATLAB-Simulink. To accurately predict the harmonic current, the flux linkage and inductance considering the rotor shaft and stator end winding leakage are analyzed. Second, an electromagnetic analysis is performed by applying the harmonic current calculated according to the load conditions for each operating speed from the two-dimensional finite element (FE) analysis. The electromagnetic losses generated when the harmonic current is applied are then compared with the electromagnetic losses generated when a sinusoidal current is applied, and the loss components are comprehensively analyzed. The stator copper losses were divided into DC and AC copper losses and the sleeve and PM (which are conductive materials) were expressed as rotor eddy current losses. In particular, the stator core loss was derived using the modified Steinmetz equation by analyzing the flux density inside the stator for each harmonic. Finally, to verify the validity of the proposed hybrid analysis, which combines the stator copper loss and rotor eddy current loss derived from the FE analysis and the proposed core loss analysis, prototypes and an experimental setup were constructed.

To measure the mechanical losses, two prototypes were manufactured that depended on the presence or absence of PM magnetization, and no-load core losses and mechanical losses were separated through a no-load test. By applying the measured mechanical loss, the analysis results and experimental results were compared and the validity of the proposed analysis method was determined from the presented results.

2. High-Speed Permanent Magnet Synchronous Motor with SVPWM Inverter

2.1. Design Specifications of the HPMSM

Figure 1 displays the HPMSM with its concentrated winding in two parts: the rotor and stator assemblies. The rotor assembly contains PMs and a shrink-fit sleeve, while the stator assembly contains a stator core, winding, and housing. Table 1 presents the design specification of a manufactured HPMSM with a concentrated winding.
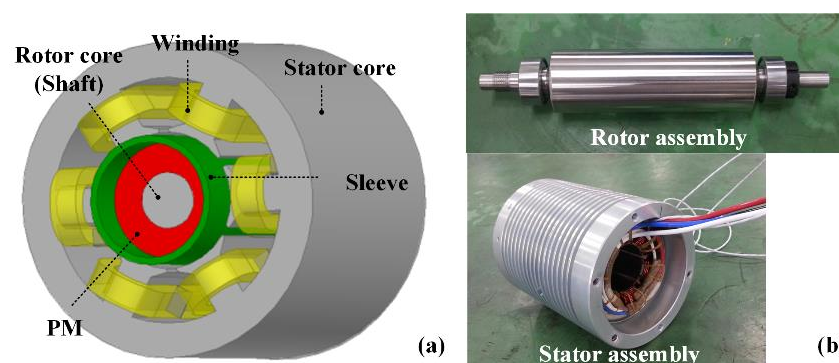

Figure 1. Structure of the HPMSM: (**a**) analysis model and (**b**) prototype.

As shown in Table 2, the flux linkage, inductance, and resistance of the HPMSM were calculated using commercial FE analysis software (ANSYS Electronics Desktop 2022R2) and then applied to the dynamic modeling. To improve the accuracy of harmonic current prediction, flux linkage and inductance were analyzed considering the effects of the stator end winding and rotor shaft.

Table 1. Specifications of the HPMSM.

Parameters	Values	Parameters	Values
Pole number	2	Shaft outer diameter	16 mm
Slot number	6	Stack length	84 mm
Slot opening	3 mm	Airgap length	1 mm
Rotor outer diameter	37 mm	Stator outer diameter	90 mm
PM thickness	8.5 mm	Turns per phase	72
Sleeve thickness	2 mm	Parallel branches	2
Material of stator core	20PN1500	Material of PM	Sm2Co17
Material of shaft core	STS420J2	Material of sleeve	Inconel

Table 2. Electrical circuit parameters of the HPMSM.

Parameters		Analytical and FE Analysis	Measurement
Phase resistance [mΩ]		52.7	53.2
Inductance [mH]	Self	0.334	0.34
	Mutual	0.23	0.26
Fluxlinkage [Wb]		0.0389	0.0387

2.2. Dynamic Simulation Model with HPMSM and SVPWM Inverter

In HPMSM drive systems, the motor is driven by a PWM voltage source inverter to achieve vector control. The PWM method chops the DC voltage to obtain the desired average current over a PWM period. In addition to the desired average voltage, the PWM method generates a high-frequency current harmonic by the carrier frequency. This high-frequency current harmonic is very important in HPMSMs because it induces AC losses in the windings, core losses in the electrical steel, and eddy current losses in both the PM and the sleeve.

To consider the previously mentioned effects, a block diagram of the dynamic simulation can be constructed, as shown in Figure 2. The overall system includes two closed loops: an inner current control loop and an outer speed control loop. When a reference speed (N_s*) is given, the system automatically compares it with the actual speed (N_s). When N_s or the load torque (T_L) changes, the reference *d-q* currents I_d^{e*} and I_q^{e*} immediately adjust the speed and torque. Simultaneously, N_s should equal N_s* and the motor operation achieves a steady-state characteristic. Moreover, the current loop forces the actual currents to track the commanded current [8–10]. The purpose of the PWM inverter is to implement a sinusoidal three-phase AC voltage using the DC link voltage. To obtain a sinusoidal three-phase voltage from a three-phase PWM inverter, a carrier wave is implemented from the time counter of the digital signal processor (DSP) and is compared with the reference voltage signal. The frequency of the carrier wave is known as the carrier frequency. Due to the limitations of power electronics and material technology, the carrier frequency is limited to 10–15 kHz. Therefore, the current contains harmonic components, and the main harmonic orders of the phase currents are described in [5]. For example, in the case of 25,000 rpm and f_c = 12 kHz, f_c/f_0 = 24. The orders of the main harmonics are presented in Table 3.

Based on Figure 2, dynamic simulation of the HPMSM was implemented using MATLAB Simulink. The operating current applied to the stator winding by the PWM inverter according to various speed and load conditions can be obtained through a dynamic simulation. The experimental setup to verify the validity of the presented dynamic modeling and proposed analysis of the HPMSM is presented in Figure 3, comprising the driving and load HPMSM, inverter with controller, equipment for measurements (such as torque sensor and power analyzer), and resistive load.
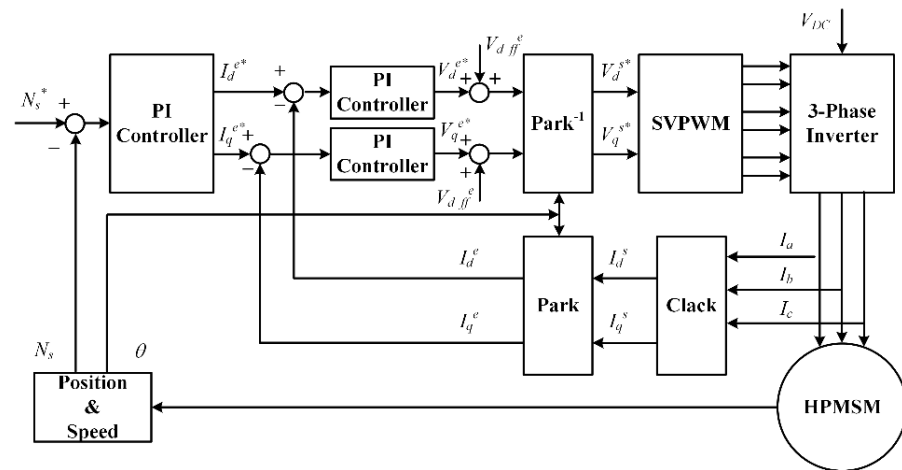
Figure 2. Block diagram for dynamic simulation of the HPMSM.

Table 3. Major harmonics order of phase current by PWM.

i	$(2i - 1)f_c/f_0 - 2$	$(2i - 1)f_c/f_0 + 2$	$(2i - 1)f_c/f_0 - 4$	$(2i - 1)f_c/f_0 + 4$
1	26.8	30.8	24.8	32.8
2	84.4	88.4	82.4	90.4
3	142	146	140	148
i	$2i\,f_c/f_0 - 1$	$2i\,f_c/f_0 + 1$	$2i\,f_c/f_0 - 5$	$2i\,f_c/f_0 + 5$
1	56.6	58.6	52.6	62.6
2	114.2	116.2	110.2	120.2
3	171.8	173.8	167.8	177.8

where i = 1, 2, 3, ..., f_c is the carrier frequency and f_0 is the fundamental frequency [5].
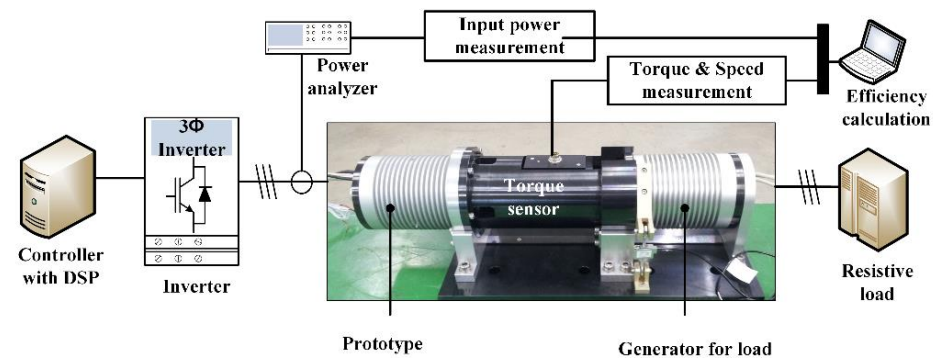

Figure 3. Performance evaluation system.

Figure 4 shows the current waveform (measured experimentally) and the predicted current waveform through the dynamic simulation under the rated load condition.

Compared with reference [10], the current harmonics were accurately predicted by accurately analyzing the flux linkage and inductance considering the stator end winding and rotor shaft. The estimated current was similar to the measured current in terms of the magnitude and harmonic components. From a comparison of the analysis results and experimental results, the phase current obtained through the dynamic simulation presented in this paper was considered valid. When the rotor speed reached the steady-state speed, the steady-state current was measured and the current profiles for all operating conditions were obtained. The operating current (including harmonics) is very useful when analyzing the electromagnetic losses of HPMSMs.
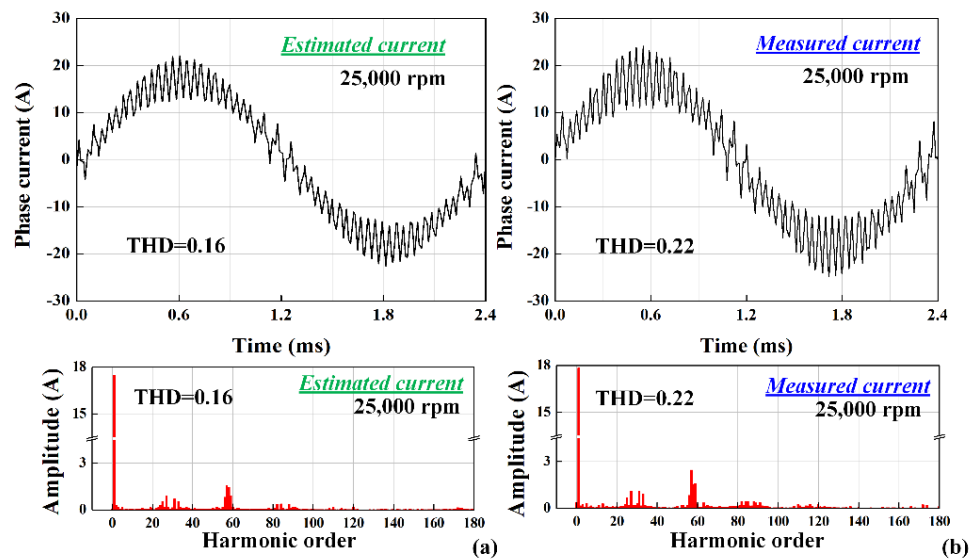
Figure 4. Comparison of current waveforms and fast Fourier transform (FFT) analysis results: (**a**) estimated and (**b**) measured currents.

3. Electromagnetic Loss Components with Harmonic Current

In this paper, an electromagnetic loss analysis was performed according to the application of the sinusoidal and harmonic currents to the HPMSM. By applying the current predicted from the dynamic model to the time-stepping FE model, the copper losses of the stator, core losses of the stator, and eddy current losses of the rotor were calculated.

3.1. Copper Losses in the Stator Winding

Copper losses in the stator winding can be divided into DC and AC losses. Copper losses due to DC resistance can be expressed as follows according to the magnitude of the current (I_{ph}), DC resistance (R_{dc}), and number of phases (m):

$$P_{cu,DC} = mI_{ph}^2 R_{dc}, \tag{1}$$

where the DC resistance is determined by the winding specifications, stator dimensions, and operating temperature [11,12].

The AC copper losses are affected by the frequency of the current applied to the stator. The skin effect can be explained as follows: when the frequency of the current flowing in the conductor increases, the current concentrates on the surface of the conductor, which reduces the effective area of the conductor, increasing the copper loss. The skin depth representing the effective radius of the conductor can be expressed by the frequency of the current, the conductivity of the conductor, and the permeability of the vacuum [12].

$$\delta = \sqrt{\frac{1}{\pi f \mu_0 \sigma}}, \tag{2}$$

where f is the frequency of the current, m_0 is the permeability of the vacuum, and s is the electrical conductivity of the conductor.

The proximity effect occurs when there are two or more conductors. The analytical formula for the AC loss analysis considering the proximity effects of the conductors in HPMSMs is as follows [12]:

$$P_{cu,AC} = P_{cu,DC}(k_d - 1), \tag{3}$$

$$k_d = \varphi(\xi) + \left[\frac{m^2 - 1}{3} - \left(\frac{m}{2}\sin\left(\frac{\gamma}{2}\right)\right)^2\right] + \psi(\xi), \tag{4}$$

$$\varphi(\xi) = \xi \frac{\sinh(2\xi) + \sin(2\xi)}{\cosh(2\xi) - \cos(2\xi)}, \tag{5}$$

$$\psi(\xi) = 2\xi \frac{\sinh(\xi) - \sin(\xi)}{\cosh(\xi) + \cos(\xi)}. \tag{6}$$

Here, x represents the effective conductor height considering the skin depth; g represents the phase angle difference between the upper and lower layers in a double-layer winding arrangement; m is the total number of identical conductors in the layers; and k_d is a coefficient indicating the magnitude of the total copper loss compared to the DC copper loss.

Although the analytical method of studying AC losses according to a single frequency increase has been employed [13–17], AC losses due to the magnetic field caused by the PM and harmonic current of the stator winding should be analyzed through an electromagnetic analysis.

Figure 5 displays the flux line and current density of a stator winding according to the applied current waveform. The distribution of the current density is different for each conductor according to the magnetic flux line, and the distribution of the current density differs significantly when a harmonic current is applied. Since the current is not uniformly distributed in the conductor, copper losses increase significantly when a harmonic current is applied to the HPMSM, as shown in Figure 6.
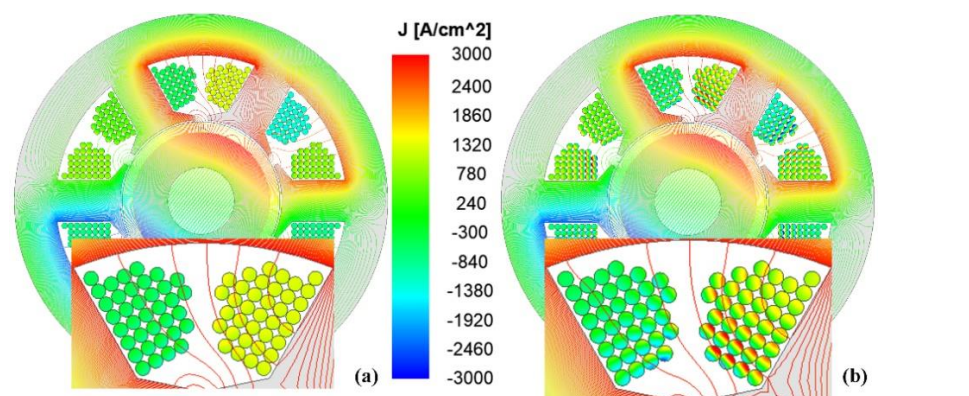

Figure 5. Distribution of magnetic flux and current density in the stator winding according to the current waveform: (**a**) sinusoidal and (**b**) PWM current.
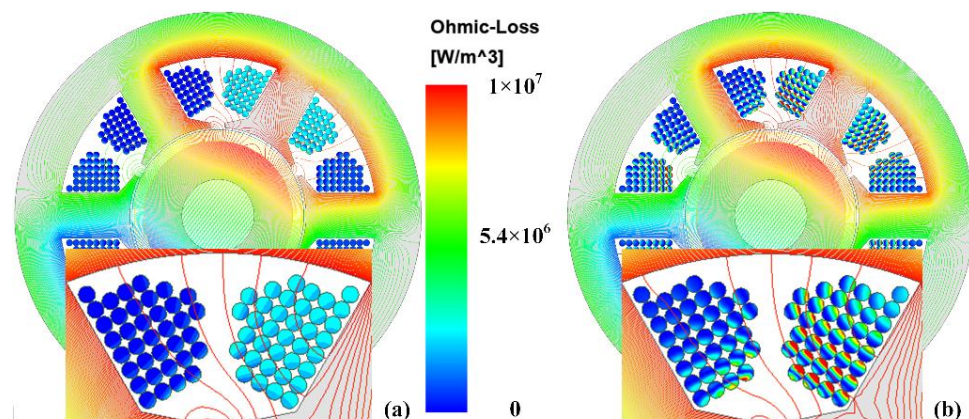

Figure 6. Distribution of copper loss density in the stator winding according to the current waveform: (**a**) sinusoidal and (**b**) PWM current.

3.2. Eddy Current Losses in the Rotor Sleeve and PM

As mentioned previously, the PM material is Sm2Co17, the retaining sleeve material is Inconel 718, and their conductivities are 1.212×10^6 and 8.345×10^5 S/m, respectively.

Eddy current losses in the rotor are caused by the time-varying magnetic vector potential in the conductive material, while there are three causes of the time-varying magnetic vector potential [12,18,19]. First, the spatial harmonics of the magnetic flux density generated from the PM are distorted by the tooth-slot structure, which generates eddy currents. Second, the distortion component of the spatial harmonics of the magnetomotive force generated from the stator windings by the stator winding arrangement also causes eddy currents. Finally, the current applied to the stator with high-order time harmonics by the PWM inverter causes eddy currents in the rotor region.

The eddy current losses generated in the rotor of an HPMSM can be calculated as follows [12,18,19]:

$$P_{rotor} = \sum_k \int_{V_{rot}} \frac{J_k^2}{\sigma_{rot}} dV_{rot}, \tag{7}$$

where σ_{rot} is the conductivity of different parts of the rotor, J_n is the eddy current density of the kth time harmonic, and V_{rot} is the volume of the material.

Since eddy current losses caused by the slot opening under no-load conditions are almost negligible, we analyzed the eddy current loss of the HPMSM to which the sinusoidal and harmonic currents have been applied. The phenomena described previously can be demonstrated by the eddy current distribution in the rotors with the current harmonics, as displayed in Figure 7.
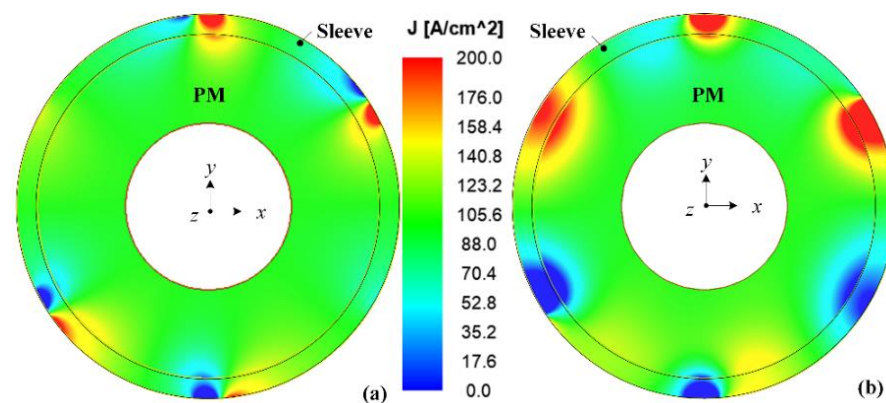

Figure 7. Distribution of eddy current density according to the current waveform: (**a**) sinusoidal and (**b**) PWM current.

As shown in Figure 1, the length (l_{act}) of the rotor sleeve is designed to be longer in the axial direction than the length (l_{stk}) of the stator core of the HPMSM to couple with the shaft. Since the length of the sleeve does not affect the analysis of the electromagnetic performance (such as back electromotive force, inductance, and torque), the results for the 2D and 3D electromagnetic analyses are similar. However, since the current path changes in the rotor loss analysis, a 3D analysis is required to analyze the eddy current losses. The analysis of the eddy current loss density according to the sinusoidal current and PWM current applied to the stator winding' is displayed in Figure 8. As described previously, when the PWM current is applied to the stator winding, the eddy current loss is significantly enhanced due to the higher-order time harmonics.

It is important to note that it is not feasible to analyze the eddy current losses using direct 3D FE analysis for the many operating points. Therefore, we performed the eddy current loss analysis according to the operating point of the HPMSM by applying a semi-3D analysis method that combines the results of the simplified static FE analysis and the 2D eddy current analysis results to predict the eddy current losses of the rotor [20].
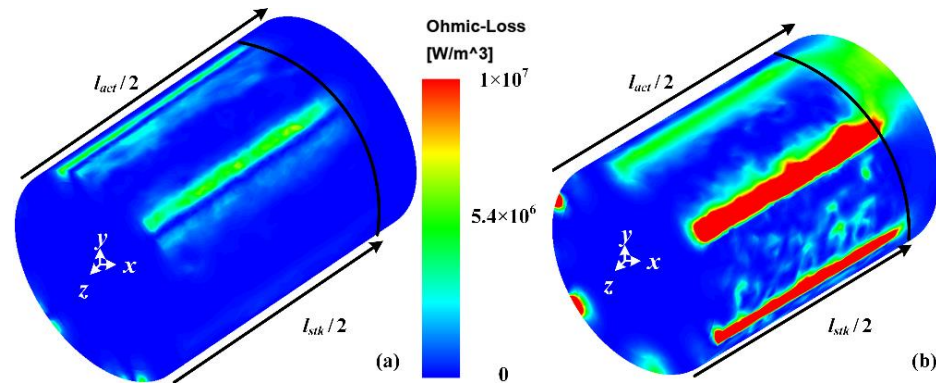
Figure 8. Distribution of eddy current loss according to the current waveform: (**a**) sinusoidal and (**b**) PWM current.

3.3. Core Losses in the Stator Core

Stator core losses consist of hysteresis losses, eddy current losses, and excess eddy current losses [21–25], which we analyzed by using the modified Steinmetz method. Figure 9 shows the calculation process of the stator core loss considering the magnetic field behavior and harmonics. Here, P2 and P4 of the shoe region, P2 of the tooth region, and P1 and P8 of the yoke region represent the analysis points of the magnetic flux density, which were arbitrarily selected in each region of the stator.
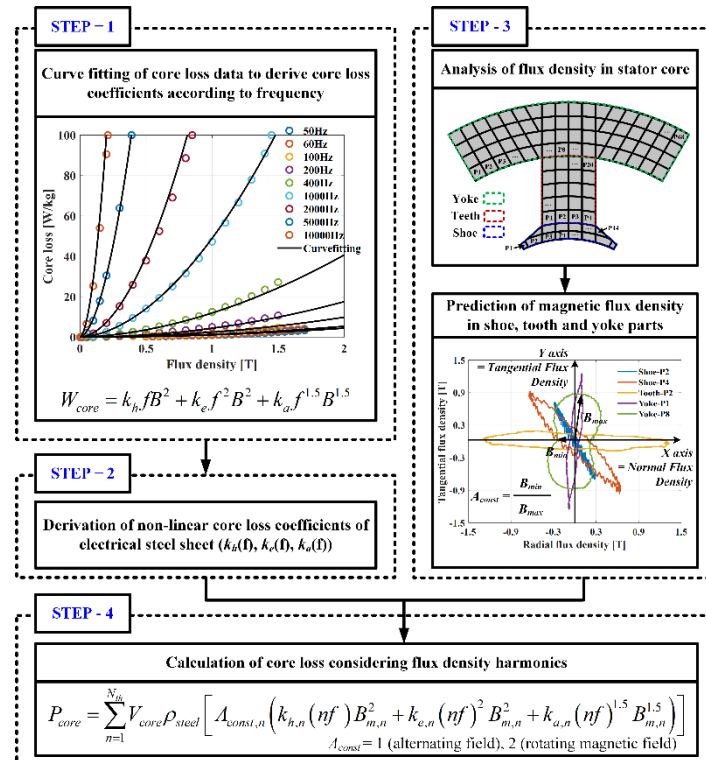

Figure 9. Calculation process of core losses considering magnetic field behavior and harmonics.

First, curve fitting was performed on core loss data according to the magnetic flux density and the frequency provided by electric steel manufacturers [21]. Second, the hysteresis loss coefficient (k_h), eddy current loss coefficient (k_e), and excess eddy current loss coefficient (k_a) were derived as a function of the frequency [22,23]. Third, the magnetic flux density in the stator shoe, tooth, and yoke regions was analyzed according to the sinusoidal and harmonic currents applied to the stator winding. As shown in Figure 10, the elliptic loci of the flux density in the normal and tangential directions were derived.
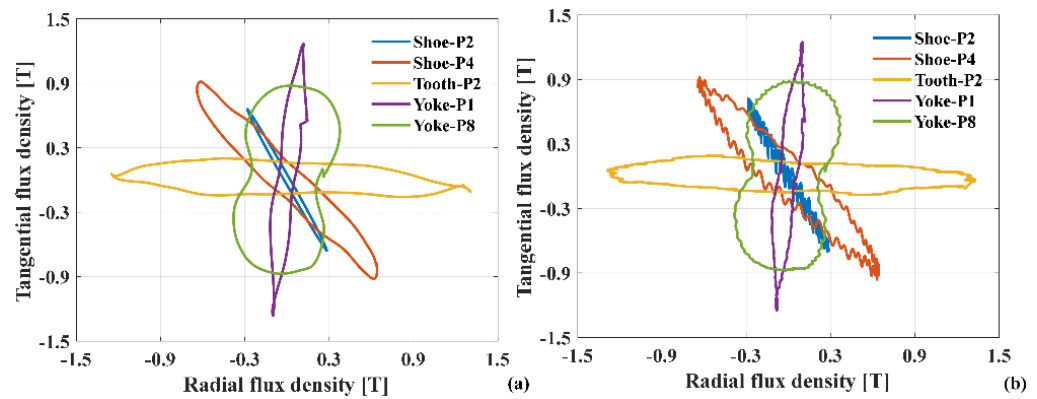
Figure 10. Elliptic loci of flux density in the normal and tangential directions: (**a**) sinusoidal and (**b**) PWM current applied to the stator winding.

The alternating and rotating magnetic fields can be determined from the major and minor axes of the elliptic magnetic flux density, and the axis ratio (B_{min}/B_{max}) can be calculated according to the loci of the flux density through the FFT analysis for each harmonic [22,23]. When the axis ratio is >0.1, it is considered a rotating magnetic field, and when the axis ratio is ≤0.1, it is considered an alternating magnetic field.

Finally, the modified Steinmetz equation, which considers the flux density behavior and the harmonic components, is expressed as follows [22–25]:

$$P_{core} = \sum_{n=1} V_{core}\rho_{steel} \left[A_{const,n} \left(k_{h,n}(nf)B_{m,n}^2 + k_{e,n}(nf)^2 B_{m,n}^2 + k_{a,n}(nf)^{1.5} B_{m,n}^{1.5} \right) \right]. \qquad (8)$$

Here, V_{core} is the volume of the stator core, ρ_{steel} is the mass density of the electrical steel sheet, n represents the harmonic order, and A_{const} compensates for any inaccuracies in the core loss coefficients derived based on the Epstein data. The values of A_{const} are 1 and 2 in the alternating and rotating magnetic field regions, respectively.

Figures 11 and 12 display the core loss results according to the analysis region (stator shoe, tooth, and yoke) and main frequency components when the sinusoidal and harmonic currents are applied to the HPSMM. The core loss of an HPMSM to which a sinusoidal current is applied has a significantly higher fundamental component value compared to other harmonics.
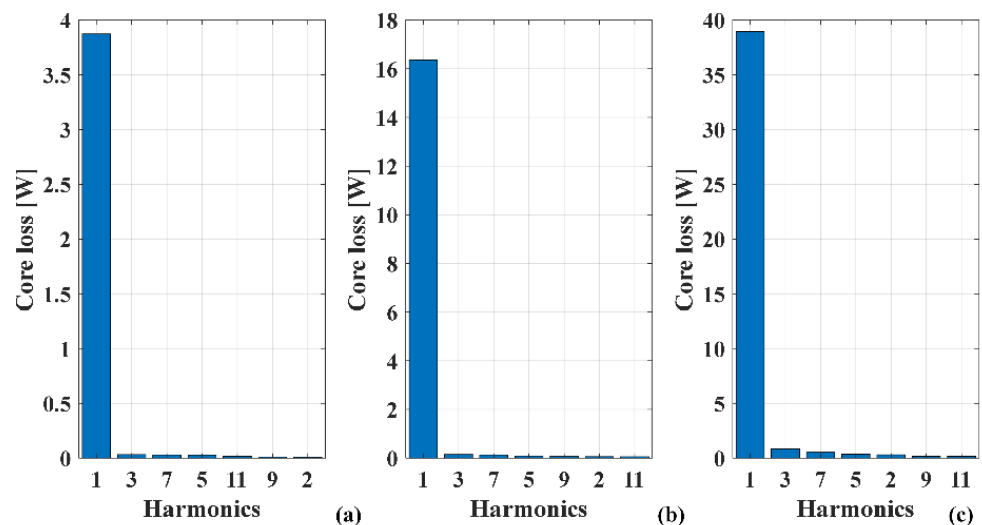

Figure 11. Analysis results of core loss according to magnetic flux density harmonics with sinusoidal current applied to the stator winding: (**a**) stator shoe, (**b**) stator tooth, and (**c**) stator yoke.
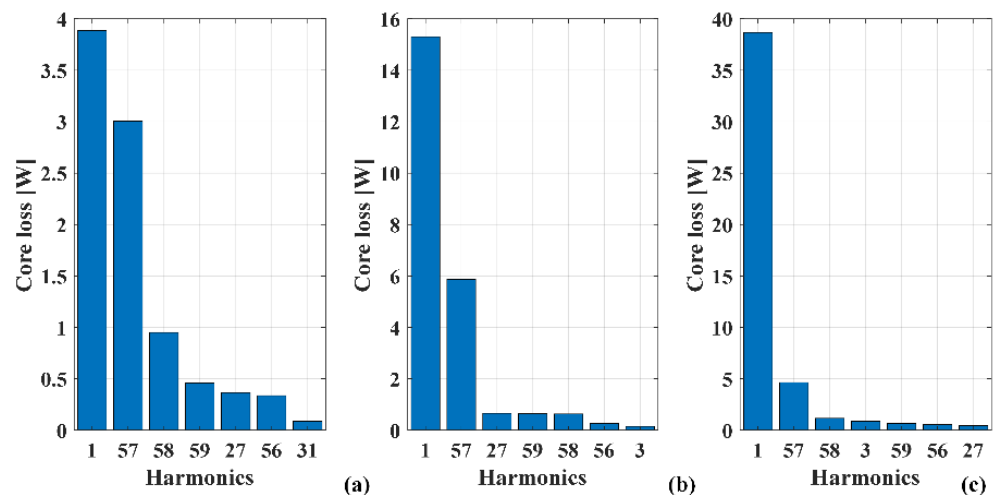
Figure 12. Analysis results of core loss according to magnetic flux density harmonics with PWM current applied to the stator winding: (**a**) stator shoe, (**b**) stator tooth, and (**c**) stator yoke.

When the harmonic current is applied to an HPMSM, the fundamental current component and the 27th, 57th, 58th, and 59th orders included in the current harmonic cause significant core losses in each region. Moreover, from the analysis results, the electromagnetic losses (including stator copper losses, core losses, and rotor eddy current losses) increase significantly when the harmonic current is applied to HPMSMs.

4. Experimental Setup and Performance Evaluation

To verify the proposed analysis method, a back-to-back experimental setup was constructed using manufactured HPMSMs and an inverter, load generator and load resistors, speed and torque sensors, an oscilloscope, and a power analyzer. In particular, to measure the mechanical losses, a rotor with a magnetized PM and a rotor with a non-magnetized PM were manufactured and assembled with a stator.

4.1. No-Load Test

A no-load test was performed to verify the mechanical and no-load core losses according to the speed of the manufactured HPMSM. The experimental system for conducting the no-load test is presented in Figure 13 [26,27]. The HPMSMs with magnetized and non-magnetized PMs were rotated according to the speed of the driving motor, and the generated torque and speed were measured using a torque-speed sensor with a power analyzer.
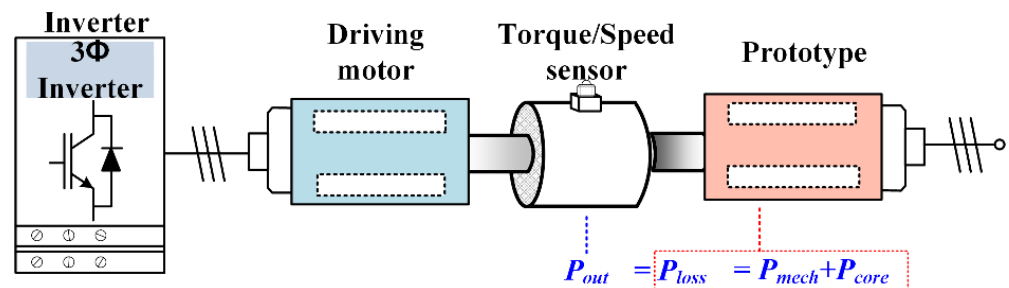

Figure 13. Schematic of performance evaluation system for the no-load test.

Figure 14 displays the loss characteristics according to the speed under the no-load condition. First, experiments were conducted in the no-load condition on a rotor with a non-magnetized PM. Here, only mechanical losses (P_{mech}) occurred in the HPMSM because there was no magnetic field in the rotor. Then, experiments were performed under no-load conditions on a rotor with a magnetized PM, and the no-load loss (P_{noload}) was measured.
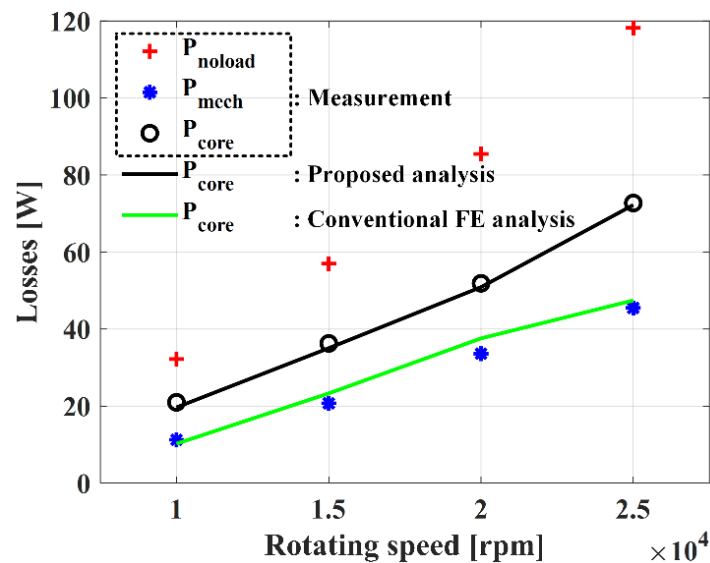
Figure 14. Mechanical and core losses under no-load conditions.

When rotating an HPMSM with a magnetized PM, the core loss (P_{core}) under no-load conditions (predicted from the measured torque and speed) can be expressed as the no-load loss (P_{noload}) and the mechanical loss (P_{mech}).

$$P_{core} = P_{noload} - P_{mech}. \tag{9}$$

Since the HPMSM with non-magnetized PM has no magnetic field in the rotor, the measured no-load loss represents the mechanical loss (P_{mech}). To verify the validity of the proposed core loss analysis, the commercial FE analysis results, proposed loss analysis results, and experimental results were compared according to the speed, as shown in Figure 14. Since the mechanical loss measured according to the speed from the experimental method proposed from the experimental results was valid, it was applied equally to the load analysis and experiment to measure the overall loss and efficiency.

4.2. Load Test

The mechanical loss according to speed was measured from the no-load experiment. Due to the range and capacity limitations of the load resistors connected to the generator, the output was only measured at one point for each speed. The maximum current of an inverter was 20 A_{rms}, and the resistive load for each phase was fixed at 6.67 Ohm. The load test was performed using the performance evaluation system depicted in Figure 3.

As shown in Figure 15 and Table 4, the input current waveform, input power, and output power from the load test were measured for each speed.

Table 4. Measurement results of input power, output, mechanical loss, and electromagnetic loss.

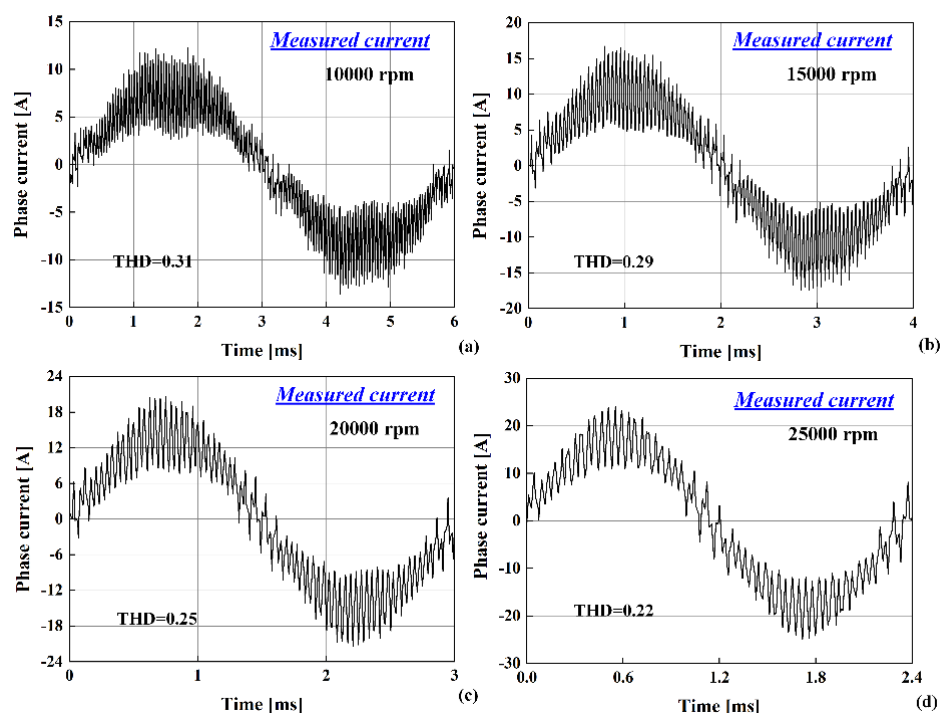| Speed [rpm]	Input Power [W]	Output Power [W]	Mech. Loss [W]	Elec. Loss [W]
10,000	547.44	477.00	11.23	59.21
15,000	1138.90	1015.48	20.70	102.72
20,000	1951.81	1757.48	33.60	160.73
25,000	2865.47	2563.00	45.47	257.00

Figure 15. Measured input current under load conditions: (**a**) 10,000 rpm, (**b**) 15,000 rpm, (**c**) 20,000 rpm, (**d**) 25,000 rpm.

5. Results and Discussion

Figure 16 presents a comparison of the results of the loss components according to the current input condition and speed with the experimental results. The electromagnetic loss analysis was performed through the proposed method by combining the FE analysis and the dynamic model. However, the mechanical loss could not be predicted through this analysis. Therefore, the mechanical losses according to the speed obtained through the no-load test were applied to the analysis and experimental results to compare the total losses. The loss analysis is represented by the stator copper losses, core losses, and rotor losses. The stator copper losses were divided into DC and AC copper losses, and the AC loss component due to the harmonics was analyzed by directly modeling the stranded conductor of the winding. The AC copper loss was calculated directly from the FE analysis, and the DC copper loss was analytically calculated considering the temperature and the length of the end winding. The eddy current losses in the rotor were calculated in the sleeve and PM, and a loss analysis was performed considering the 3D effect using a semi-3D analysis technique. The eddy current loss considering the 3D effect was calculated by combining the 2D transient FE analysis and the 3D static FE analysis. Finally, the core loss of the stator was classified into rotating and alternating magnetic fields according to the harmonic order and analysis area by analyzing the magnetic flux density of the analysis area over time and applying FFT. The core losses of the stator were calculated using the modified Steinmetz equation. All the FE analyses were performed based on 2D analyses. For the 3D effect, the length of the end winding was considered for the stator DC copper losses, and the PM and sleeve of the rotor were compensated for by applying the semi-3D technique considering the axial length [12]. When the sinusoidal and harmonic currents were applied to the HPMSM, the DC copper losses were the same for both. However, the AC copper losses drastically increased due to the PWM current having high-order time harmonics. Moreover, when the sinusoidal and harmonic currents were applied to the HPMSM, the difference in core losses at low speeds was relatively small (11%). In contrast, the core losses of the HPMSM caused by the PWM current increased significantly as the speed increased (30%). Compared to the eddy current losses of the rotor when a sinusoidal current was applied to the HPMSM, when PWM current was applied, the ratio

of the eddy current losses of the rotor increased by approximately 70% at every operating point. As shown in Table 5, we confirmed that the loss results derived by the proposed analysis agreed well with the experimental results. It was also possible to accurately predict and measure the efficiency of the HPMSM using the proposed analysis and experimental evaluation, as shown in Table 5. Additionally, Table 5 shows the error by comparing the loss and efficiency of the analysis results with the experimental results.
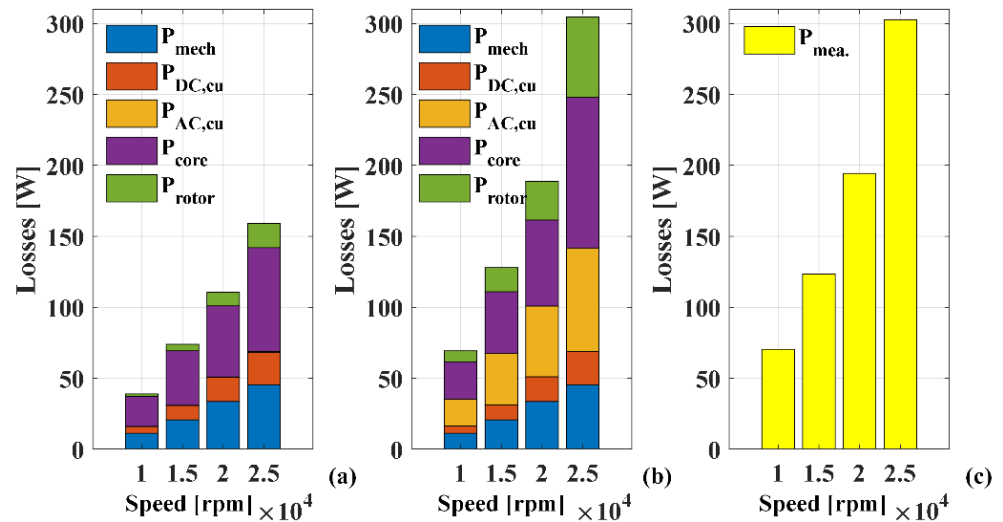

Figure 16. Comparison of analysis and experimental results according to speed and loss components: (**a**) analysis with sinusoidal current, (**b**) analysis with PWM current, and (**c**) experiment.

Table 5. Comparison of power loss and efficiency results according to operating conditions.

Speed (rpm)	Torque (N·m)	Hybrid Analysis with Sinusoidal Current		Hybrid Analysis with Harmonic Current		Experiment	
		Loss [W]	Eff. [%]	Loss [W]	Eff. [%]	Loss (W)	Eff. (%)
10,000	0.45	38.94 (44.72)	92.24 (5.86)	69.30 (1.62)	87.04 (0.1)	70.44	87.13
15,000	0.65	73.90 (40.12)	93.24 (4.58)	127.91 (3.64)	88.85 (0.35)	123.42	89.16
20,000	0.84	110.70 (43.06)	94.11 (4.52)	188.80 (2.85)	90.34 (0.33)	194.33	90.04
25,000	0.98	159.14 (47.39)	94.15 (5.27)	304.58 (0.69)	89.37 (0.08)	302.47	89.44

6. Conclusions

This paper presented a comprehensive analysis of the electromagnetic losses of HPMSMs considering the current harmonics generated from the SVPWM inverter. In addition, a dynamic model and a block diagram combining the SVPWM and HPMSM were presented to predict the operating characteristics and harmonic currents. The harmonics current was accurately predicted by accurately deriving and inputting the electric circuit parameters of the HPMSM considering the increase in end inductance by the shaft and the decrease in the linkage by the PM. The predicted current waveform was applied to the FE analysis model of the HPMSM to calculate the stator DC and AC copper losses. The AC copper losses increased significantly due to the current harmonics. To calculate the eddy current losses in the rotor, a rotor eddy current loss analysis was performed considering the actual length of the sleeve using a semi-3D analysis technique based on the 2D eddy current loss analysis and static 3D magnetic field analysis. When analyzing the core losses in the stator, the magnetic field behavior was analyzed in all areas of the stator, and the core

loss was derived by separating the rotating and alternating magnetic fields and the magnetic field caused by the harmonics. The core loss considering the magnetic field behavior characteristics according to the harmonic order of the magnetic field was larger than that of the existing FE analysis, and the validity of the proposed analysis method was verified through the experimental results under no-load conditions. To verify the proposed hybrid analysis, an experimental setup was constructed and prototypes were manufactured. The validity of the proposed analysis was affirmed through the experimental results. Finally, the loss analysis and experimental method for HPMSMs proposed in this study can be employed for various electric motors.

Author Contributions: Conceptualization, K.-H.S., J.-H.L. and J.-Y.C.; methodology, K.-H.S., H.-W.C. and J.-H.L.; software, K.-H.S. and J.-H.L.; validation, K.-H.S., J.-H.L. and J.-Y.C.; writing—original draft preparation, K.-H.S., H.-W.C. and J.-Y.C.; writing—review and editing, K.-H.S. and J.-Y.C.; supervision, S.S. and K.-H.S.; funding acquisition, S.S. and K.-H.S. All authors have read and agreed to the published version of the manuscript.

Data Availability Statement: Not applicable.

Conflicts of Interest: The authors declare no conflict of interest.

References

1. Gerada, D.; Mebarki, A.; Brown, N.L.; Gerada, C.; Cavagnino, A.; Boglietti, A. High-speed electrical machines: Technologies, trends, and developments. *IEEE Trans. Ind. Electron.* **2013**, *61*, 2946–2959. [CrossRef]
2. Dong, J.; Huang, Y.; Jin, L.; Lin, H. Comparative study of surface-mounted and interior permanent-magnet motors for high-speed applications. *IEEE Trans. Appl. Supercond.* **2016**, *26*, 5200304. [CrossRef]
3. Bramerdorfer, G.; Tapia, J.A.; Pyrhönen, J.J.; Cavagnino, A. Modern Electrical Machine Design Optimization: Techniques, Trends, and Best Practices. *IEEE Trans. Ind. Electron.* **2018**, *65*, 7672–7684. [CrossRef]
4. Schwager, L.; Tuysuz, A.; Zwyssig, C.; Kolar, J.W. Modeling and comparison of machine and converter losses for PWM and PAM in high-speed drives. *IEEE. Trans. Ind. Appl.* **2014**, *50*, 995–1006. [CrossRef]
5. Zhang, C.; Chen, L.; Wang, X.; Tang, R. Loss Calculation and Thermal Analysis for High-Speed Permanent Magnet Synchronous Machines. *IEEE Access* **2020**, *8*, 92627–92636. [CrossRef]
6. Jumayev, S.; Merdzan, M.; Boynov, K.; Paulides, J.; Pyrhönen, J.; Lomonova, E. The effect of PWM on rotor eddy-current losses in high-speed permanent magnet machines. *IEEE Trans. Magn.* **2015**, *51*, 8109204. [CrossRef]
7. Miyama, Y.; Hazeyama, M.; Hanioka, S.; Watanabe, N.; Daikoku, A.; Inoue, M. PWM Carrier Harmonic Iron Loss Reduction Technique of Permanent Magnet Motors for Electric Vehicles. *IEEE Trans. Ind. Appl.* **2016**, *52*, 2865–2871. [CrossRef]
8. Gu, C.; Wang, X.L.; Deng, Z.Q. Evaluation of three improved space-vector-modulation strategies for the high-speed permanent magnet motor fed by a SiC/Si hybrid inverter. *IEEE Trans. Power Electron.* **2021**, *36*, 4399–4409. [CrossRef]
9. Zhuo, L.; Yang, D.; Sun, R.; Sun, L.; Zou, J. Accurate Calculation of Iron Loss of High-Temperature and High-Speed Permanent Magnet Synchronous Generator under the Conditions of SVPWM Modulation. *Energies* **2022**, *15*, 2315. [CrossRef]
10. Woo, J.H.; Bang, T.K.; Lee, H.K.; Kim, K.H.; Shin, S.H.; Choi, J.Y. Electromagnetic characteristic analysis of high-speed motors with rare-earth and ferrite permanent magnets considering current harmonics. *IEEE Trans. Magn.* **2021**, *57*, 8201805. [CrossRef]
11. Wrobel, R.; Mellor, P.H.; Popescu, M.; Staton, D.A. Power Loss Analysis in Thermal Design of Permanent-Magnet Machines—A Review. *IEEE Trans. Ind. Appl.* **2016**, *52*, 1359–1368. [CrossRef]
12. Huynh, C.; Zheng, L.; Acharya, D. Losses in High Speed Permanent Magnet Machines Used in Microturbine Applications. *J. Eng. Gas Turbines Power* **2008**, *131*, 022301. [CrossRef]
13. Birnkammer, F.; Chen, J.; Pinhal, D.B.; Gerling, D. Influence of the Modeling Depth and Voltage Level on the AC Losses in Parallel Conductors of a Permanent Magnet Synchronous Machine. *IEEE Trans. Appl. Supercond.* **2018**, *28*, 0601705. [CrossRef]
14. Liu, J.; Fan, X.; Li, D.; Qu, R.; Fang, H. Minimization of AC copper loss in permanent magnet machines by transposed coil connection. *IEEE Trans. Ind. Appl.* **2021**, *57*, 2460–2470. [CrossRef]
15. Popescu, M.; Dorrell, D.G. Proximity Losses in the Windings of High-Speed Brushless Permanent Magnet AC Motors With Single Tooth Windings and Parallel Paths. *IEEE Trans. Magn.* **2013**, *49*, 3913–3916. [CrossRef]
16. Gonzalez, D.A.; Saban, D.M. Study of the Copper Losses in a High-Speed Permanent-Magnet Machine with Form-Wound Windings. *IEEE Trans. Ind. Electron.* **2013**, *61*, 3038–3045. [CrossRef]
17. Du, G.; Ye, W.; Zhang, Y.; Wang, L.; Pu, T. Comprehensive Analysis of Influencing Factors of AC Copper Loss for High-Speed Permanent Magnet Machine with Round Copper Wire Windings. *Machines* **2022**, *10*, 731. [CrossRef]

18. Han, T.; Wang, Y.C.; Shen, J.X. Analysis and Experiment Method of Influence of Retaining Sleeve Structures and Materials on Rotor Eddy Current Loss in High-Speed PM Motors. *IEEE Trans. Ind. Appl.* **2020**, *56*, 4889–4895. [CrossRef]

19. Kim, J.H.; Kim, D.M.; Jung, Y.H.; Lim, M.S. Design of ultra-high-speed motor for fcev air compressor considering mechanical properties of rotor materials. *IEEE Trans. Energy Convers.* **2021**, *36*, 2850–2860. [CrossRef]

20. Shin, K.; Park, H.; Cho, H.; Choi, J. Semi-three-dimensional analytical torque calculation and experimental testing of an eddy current brake with permanent magnets. *IEEE Trans. Appl. Supercond.* **2018**, *28*, 5203205. [CrossRef]

21. *Ansys GRANTA Multi Campus Solution Software*; ANSYS, Inc.: Cambridge, UK, 2022. Available online: http://www.ansys.com/materials (accessed on 15 October 2022).

22. Shin, K.H.; Hong, K.; Cho, H.W.; Choi, J.Y. Core Loss Calculation of Permanent Magnet Machines Using Analytical Method. *IEEE Trans. Appl. Supercond.* **2018**, *28*, 5205005. [CrossRef]

23. Kim, C.W.; Koo, M.M.; Kim, J.M.; Ahn, J.H.; Hong, K.Y.; Choi, J.Y. Core Loss Analysis of Permanent Magnet Synchronous Generator with Slotless Stator. *IEEE Trans. Appl. Supercond.* **2018**, *28*, 5204404. [CrossRef]

24. Zhu, S.; Cheng, M.; Dong, J.; Du, J. Core loss analysis and calculation of stator permanent-magnet machine considering dc-biased magnetic induction. *IEEE Trans. Ind. Electron.* **2014**, *61*, 5203–5212. [CrossRef]

25. Okamoto, S.; Denis, N.; Kato, Y.; Ieki, M.; Fujisaki, K. Core Loss Reduction of an Interior Permanent-Magnet Synchronous Motor Using Amorphous Stator Core. *IEEE Trans. Ind. Appl.* **2016**, *52*, 2261–2268. [CrossRef]

26. Yao, A.; Sugimoto, T.; Odawara, S.; Fujisaki, K. Core losses of a permanent magnet synchronous motor with an amorphous stator core under inverter and sinusoidal excitations. *AIP Adv.* **2018**, *8*, 056804. [CrossRef]

27. Denis, N.; Kato, Y.; Ieki, M.; Fujisaki, K. Core losses of an inverter-fed permanent magnet synchronous motor with an amorphous stator core under no-load. *AIP Adv.* **2016**, *6*, 055916. [CrossRef]